A high-rate aqueous proton battery delivering power below -78 ºC via an unfrozen phosphoric acid

*Heng Jiang, Woochul Shin, Lu Ma, Jessica J. Hong, Zhixuan Wei, Yusung Liu, Suoying Zhang, Xianyong Wu, Yunkai Xu, Qiubo Guo, Mas A. Subramanian, William F. Stickle, Tianpin Wu, Jun Lu *, Xiulei Ji**

H. Jiang, W. Shin, J. J. Hong, Dr. Z. Wei, Y. Liu, Dr. X Wu, Y. Xu, Q. Guo, Prof. M. A. Subramanian, and Prof. X. Ji

Department of Chemistry, Oregon State University, Corvallis, 97331-4003, United States

*Email: david.ji@oregonstate.edu

Dr. J. Lu

Chemical Sciences and Engineering Division and X-ray Science Division, Advanced Photon Sources, Argonne National Laboratory, Lemont, IL, 60439, United States

*Email: junlu@anl.gov

Dr. L. Ma, Dr. S. Zhang, Dr. T. Wu

X-ray Science Division, Advanced Photon Sources, Argonne National Laboratory, Lemont, Illinois, 60439, United States

Dr. W. Stickle

Hewlett-Packard Co. 1000 NE Circle Blvd., Corvallis, OR 97330, United States

Keywords: Battery, Low temperature, Proton, Phosphoric acid, Aqueous electrolyte

Abstract: The sluggish ion diffusion and electrolyte freezing with volumetric changes limit the low-T performance of rechargeable batteries. Herein, we report a high-rate aqueous proton battery (APB) operated at and below -78 ^{o}C via a 62 wt% (9.5 m) H_3PO_4 electrolyte. The APB is a rocking-chair battery that operates with protons commuting between a Prussian blue cathode and a MoO_3 anode. At -78 ^{o}C, the APB full cells exhibit non-fading cycle life for 300 cycles, high round-trip efficiency of 85%, and appreciable power performance. The APB delivers 30% of its room-temperature capacity even at -88 ^{o}C. The proton storage mechanism is investigated by *ex situ* synchrotron XRD, XAS, and XPS. EIS measurements reveal fast proton-conducting kinetics. The APB reaches a high technology readiness level, where its pouch cells demonstrate nil capacity fading at -78 ^{o}C, which offers a safe and reliable candidate for aerospace and high-atmosphere applications.

1. Introduction

Low-temperature batteries are imperative for humanity's polar activities and exploration of aerospace. The proposed settlement on Mars, where the average temperature is -63 ^{o}C, demands a powerful low-T battery for outdoor activities. However, none of the commercialized batteries can survive such low-T conditions.[1-3] Recently, progress has been made, where several non-aqueous electrolytes with low-melting points[4,5] have been identified such as liquified gas,[6,7] fluorinated solvents,[8] and ethyl acetate.[9] Yet, the safety concern, the environmental impacts, and the high cost are the inherent challenges of non-aqueous electrolytes, where these aspects are, nonetheless, the advantages of aqueous ones. There has been an entrenched assumption that aqueous electrolytes cannot support a battery's operation far below the freezing point of water.

Among aqueous batteries, APBs represent a promising solution for large-scale energy storage that are safe, powerful, and of low levelized energy cost.[10-13] In particular, APBs should be the

natural choice of low-T batteries. Low-T conditions slow down the kinetics of redox reactions due to the sluggish ion migration; however, the diffusion of protons, the smallest ionic charge carrier, can be extremely fast, *e.g.*, by the Grotthuss mechanism. For any low-T batteries, the challenge is to identify the electrolyte that offers high conductivity under low-T conductions, where such electrolytes are ideally in the liquid form. Recently, the frozen acids have been investigated as solid-state electrolytes for proton storage under low-T conditions, demonstrating the advantages of APBs in kinetics.[14-16] In this study, we selected H_3PO_4 as a liquid electrolyte for low-T APBs because 9.5 m H_3PO_4 does not freeze until -85 ^oC.

In our prior study, we reported a Turnbull's blue analogue (TBA), *i.e.*, $Cu_{II}[Fe_{III}(CN)_6]_{2/3}\cdot 4H_2O$, as an APB cathode that operates via the Grotthuss proton conduction.[13] Nevertheless, it appears that a showstopper of APBs is the lack of an anode that delivers stable cycling without being dissolved in the corrosive acid electrolytes and does not trigger severe hydrogen evolution reaction (HER). Unfortunately, most candidate anodes for APBs are metal oxides that can be corroded in strong acids, where H_2SO_4 is often the default choice. Thus, the community may have attempted to address the wrong question by looking for novel anode materials. The solution may come from abandoning the strong acids by adopting weak acids as electrolytes such as H_3PO_4.[17-19] Herein, we completed the design for a practically viable APB by using chemically pre-protonated TBA (H-TBA) as the cathode, MoO_3 as the anode, and a concentrated H_3PO_4, *i.e.*, 9.5 m H_3PO_4, as the electrolyte. The 9.5 m H_3PO_4, electrolyte not only facilitates the low-T performance of APBs but allows the MoO_3 anode and APB full cells to exhibit stable cycling performance.

2. Results and discussion

We fabricated APB full cells comprising the MoO_3 anode and chemically pre-protonated CuFe-TBA (H-TBA) as the cathode with an anode/cathode mass ratio of 2/3, as schematically shown by **Figure 1A**. This anode/cathode ratio is to purposely avoid using the capacity from the low-potential plateau of the MoO_3 anode (**Figure 2A**). The characterization and electrochemical performance of the as-prepared H-TBA are discussed in **Figure S1** and **S2**. In the full cell measurements, the current rates are calculated based on the active mass of anode, and the capacity is based on the total active mass of both electrodes, where the theoretical capacity is 55 mAh/g. The APB full cell exhibits a capacity of 46 mAh/g, where the energy density reaches 40 Wh/g based on the mass of both electrodes (**Figure S3A** and **B**). The APB full cell shows excellent rate performance at room temperature with discharge capacity values of 46, 44, 41, 38, and 34 mAh/g with roundtrip efficiencies of 84%, 84%, 82%, 77%, and 75% at the current rates of 5, 10, 20, 50, and 100 A/g, respectively, where at 100 A/g, the APB discharges in 1.2 seconds (**Figure 1B**). The CV curve of the full cell shows that the charge and discharge peaks are nearly vertically aligned at room temperature, indicating the kinetic reversibility at the full cell scale (**Figure 1C**). Furthermore, the APB demonstrates capacity retention of ~85% at 2 A/g for 1000 cycles (**Figure S3B**).

The primary focus of this study is to test the low-T performance of this APB chemistry considering that 9.5 m H_3PO_4 has an extremely low-melting temperature. At -78 ^oC, indeed, the APB delivers a discharge capacity of ~27.5 mAh/g and energy density 24 Wh/kg based on the active mass of two electrodes at the current rate of 25 mA/g, which are 55% and 60% of the capacity and energy density values at the room temperature (**Figure 1D**).[6,8,9] Of note, even at -88 ^oC that is 3 ^oC below the freezing point of 9.5 m H_3PO_4, the APB still provides 30% of its room-

temperature capacity, where the proton conduction is still viable.[19] At -78 °C, APB delivers negligible capacity fading over 300 cycles during the past 75 days, and the cell is still running (**Figure 1E**). The APB demonstrates excellent rate capability with 50% capacity retention upon raising the current rate from 25 mA/g to 400 mA/g at -78 °C (**Figure S3C**).

At -78 °C, APB shows a high round-trip efficiency of 85%, and also demonstrates an impeccable self-discharge performance with 97.9% capacity retention and 95% energy retention after 48 hrs of resting at an open-circuit voltage (**Figure 1F**).[20-22] Albeit the possible hydrogen evolution reaction (HER) on the MoO_3 anode side is avoided by the mass ratio between anode and cathode, it is still interesting to point out that the low temperature of -78 °C significantly suppresses HER, where negligible current is observed even by sweeping down to -1.5 V in linear sweep voltammetry (LSV) (**Figure S3D**).

For testing the potential commercial applications, we assembled pouch cells of APBs (see details in the experimental procedures), which exhibit 33.5 mAh/g and 18 mAh/g at -40 °C and -78 °C, respectively (**Figure 1E** and **S3E**). The pouch cells demonstrate a stable capacity of 18 mAh/g for 100 cycles at the current rate of 20 mA/g (**Figure 1F**). Overall, the concentrated electrolyte shows remarkable low-T electrochemical performances in both Swagelok® and pouch cells. **Table S1** enlists most low-T batteries reported on to date, including those employing non-aqueous electrolytes. The APB here reaches the highest technology readiness level (TRL), where its proof-of-concept full-cells in a pouch-cell configuration exhibits stable cycling performance at -78 °C, thus demonstrating the performance of the prototype in the relevant environment (TRL 6). This is the first cycling performance reported for pouch full cells at such a low temperature.

The viability of the low-T APB is based on the reversible proton-storage properties of MoO_3 in the H_3PO_4 electrolyte, where we have conducted detailed studies. Topotactic redox reactions of

proton-MoO_3 bronzes have been known for decades;[23-25] however, its properties as an electrode in APBs have only been recently demonstrated in a dilute H_2SO_4 electrolyte.[12,14] **Figure S4** shows the characterization results of MoO_3 fibers. Our results here show that the choice of the acid electrolyte profoundly transforms the behavior of the MoO_3 electrode (**Figure S5**). **Figure 2A** shows the galvanostatic charge-discharge (GCD) potential profiles of the MoO_3 electrode in 9.5 m H_3PO_4 electrolyte, where at 1 A/g or ~5 C MoO_3 exhibits a protonation capacity of 218 mAh/g. The electrode can deliver a capacity of 140 mAh/g even at 100 A/g or ~500 C with the discharge completed in 5.4 seconds. This is one of the fastest rate capability results among all metal oxide electrodes reported for proton storage.

Surprisingly, cyclic voltammetry (CV) curves collected at different scan rates suggest the proton storage in the MoO_3 electrode is entirely diffusion-controlled with the ***b***-values close to 0.5, indicative of no (pseudo)capacitive contribution (**Figure 2B**). This is in stark contrast to the Grotthuss pseudocapacitance of CuFe-TBA,[13,26] which has its ***b***-value as near unity. Note that the hydrogen-bonding network of lattice water molecules inside the defective TBA structure facilitates the fast Grotthuss proton conduction.[13] Galvanostatic intermittent titration technique (GITT) measurements reveal that the proton's diffusivity plummets when reaching the potentials corresponding to the plateaus of GCD potential profiles and the redox peaks of CV curves (**Figure 2C** and **Figure S6**). These results show that proton diffusion inside the MoO_3 lattice is slow. Despite the diffusion-controlled migration inside the lattice of MoO_3, as aforementioned, the APB's rate behavior is among the best, even at -78 ^oC.

As for the charge carriers in MoO_3, *in situ* electrochemical quartz crystal microbalance (EQCM) measurements suggest that both hydronium and proton migrate inside MoO_3. During the first cathodic scan down to -0.1 V vs Ag/AgCl (all potentials vs Ag/AgCl hereafter), the electrode

experiences a mass gain at the rate of 19.7 g/mol e^-, indicating the insertion of hydroniums. However, the subsequent anodic scan causes a mass loss at a much lower rate of 5.3 g/mol e^-, where, equivalently, 0.8 water molecules are irreversibly trapped in one formula of MoO_3, which is corroborated by the thermogravimetric analysis (TGA) (**Figure S7A** and **B**). During the second cycle of protonation/deprotonation, the closed-loop of the EQCM profile attests to the reversible mass change (**Figure 2D**). Water trapping in the lattice of MoO_3 may enhance the proton storage, particularly at low temperatures. The EQCM results demonstrate that MoO_3 is less soluble in 9.5 m H_3PO_4.

The 9.5 m H_3PO_4 is a more suitable electrolyte choice for the MoO_3 anode compared to the dilute H_3PO_4 and dilute H_2SO_4 on many fronts. The primary advantage is the better stability and longevity of the MoO_3 anode. After 200 cycles, the capacity retentions of the MoO_3 anode are 82% and 39% in 9.5 m H_3PO_4 and 1 M H_3PO_4, respectively, and their Coulombic efficiency (CE) is above 90% (**Figure S8A**), where in H_2SO_4 MoO_3's capacity fades to 10% in 200 cycles, and it also suffers from a conspicuous hydrogen evolution reaction (HER), where its CE is only 70% during cycling (**Figure S9**). The results indicate that a weaker acid electrolyte with a smaller proton concentration mitigates HER, and fewer free water molecules in the concentrated electrolyte are conducive to stable cycling of metal oxide anode. **Figure S8B** shows the significant loss of MoO_3 mass by 60% after 200 cycles in 1 M H_3PO_4 in sharp contrast of 20% mass loss in 9.5 m H_3PO_4. Note that in 9.5 m H_3PO_4, MoO_3 exhibits a capacity of 150 mAh/g above standard hydrogen electrode (SHE), where in full-cell studies, only this portion of the capacity is solicited to avoid any HER on the anode side.

The seemingly paradoxical diffusion-controlled but high-rate behavior of MoO_3 in 9.5 m H_3PO_4 suggests that protons may migrate fast in the electrolyte and across the electrode/electrolyte

interface, thus compensating for sluggish diffusion inside MoO_3. The performance comparison of MoO_3 between in 9.5 m H_3PO_4 and in 1 M H_3PO_4 may shed light on the advantages of the concentrated H_3PO_4 electrolyte. In 9.5 m H_3PO_4, the GCD profiles of MoO_3 display not only higher capacity but extremely low polarization of less than 0.03 V in contrast to 0.07 V in 1 M H_3PO_4 for the upper plateau (**Figure 2E**).

To investigate the charge transfer with respect to MoO_3, we conducted electrochemical impedance spectroscopy (EIS) measurements on a symmetrical cell, where two half-discharged MoO_3, *i.e.*, $H_{1.2}MoO_3$ electrodes serve as the working and counter electrodes (**Figure 2F**).[27-29] The diameters of the semicircles in the Nyquist complex plots mark the charge-transfer resistance (R_{ct}), which are 4.5 Ω in 9.5 m H_3PO_4 but 10.8 Ω in 1 M H_3PO_4. The results suggest that 9.5 m H_3PO_4 facilitates high proton conduction across the interface. In concentrated H_3PO_4 electrolytes, resembling the scenario of water-in-salt electrolyte (WiSE),[21] protons have incomplete solvation shells, which allows the direct interactions between protons and the MoO_3 surface, whereas in dilute acid's protons are wrapped by water molecules, forming a tetrahedron Eigen ion of $H_9O_4^+$. In addition, a concentrated H_3PO_4 comprises swarming H_3PO_4 molecules, where the direct interactions between the hydrogens of H_3PO_4 and surface oxygen atoms of MoO_3 may allow hydrogen to switch allegiance from O in H_3PO_4 to MoO_3 via the hydrogen bonding, resembling a one-step structural diffusion. This may be responsible for the fast charge transfer through the inner Helmholtz layer.[30-35]

The high-frequency x-intercept in EIS denotes the equivalent series resistance (ESR) of cells, which are 5 Ω and 19.5 Ω in 9.5 m H_3PO_4 and 1 M H_3PO_4, respectively. The disparity of ESR can be attributed to the higher conductivity of 9.5 m H_3PO_4 electrolyte than the dilute one, 0.11 S/cm vs 0.06 S/cm. Note that pure phosphoric acid is known as the most conductive substance for

protons.[36] The nearly vertical line at the low-frequency region in 9.5 m H_3PO_4 implies the fast proton conduction in 9.5 m H_3PO_4 in contrast to the sloping line in 1 M H_3PO_4.

The electrochemical results of MoO_3 in combination with the full cell performance of APBs reveal that even though the anode of MoO_3 functions by the diffusion-controlled kinetics of proton storage, the overall rate capability of proton storage can be secured by the fast interface charge transfer and excellent proton conduction in the electrolyte. Therefore, the performance of the MoO_3 electrode still suffices the needs of the APB full cells at extremely low temperatures.

The proton insertion mechanism is further described in **Figure 3**. We measured *ex situ* synchrotron X-ray diffraction (XRD) at different state of charge (SOC) to investigate the structural evolution upon proton (de)insertion (**Figure 3C** and **D**). The (004) peak shifts to the left, which suggests the interlayer expansion due to the water insertion during the first protonation. From pristine SOC to -0.5 V, the right shift of the (100) peak suggests the contraction of the Mo-O-Mo (corner-sharing) bonds along ***a*** axis; the opposite left shift of the (020) peak results in the extension of the edge-sharing Mo-O-Mo chains along ***b*** axis. The opposite phenomena indicate that the protons insert and migrate by forming O-H bonds with terminal O atoms. The inserted proton attracts the terminal O atoms on the neighboring layers to cause the shrinking of the (100) planes.[37] Moreover, the reduction of Mo weakens the interaction between Mo atoms and edge-shared bridging O atoms, thus expanding the (020) planes.

We conducted XPS, where the XPS data of discharged MoO_3 suggests the decrement of Mo's oxidation state from +6 to +4.55 upon proton insertion (**Figure 3E**). However, after a full charge, Mo's oxidation state was only raised to +5.5, which suggests the trapping of protons inside the structure in the first cycle, corroborating the electrochemical data.[12]

X-ray absorption spectroscopy (XAS) is sensitive to the local atomic and bond environment, which is conducted to analyze the impacts of the solvated proton insertion further. In the extended X-ray absorption fine structure (EXAFS) spectroscopy, similar as standard commercial MoO_3, the pristine sample demonstrates three main correlations at ~ 1.2 Å,~ 1.8 Å, and ~3.2 Å, corresponding to distances of Mo-O terminal, Mo-O bridging (edge-shared and corner-sharing oxygen), and Mo-Mo distance, respectively (**Figure 3F**).[38,39] During the protonation process, the new peak appeared below 1 Å is assigned to the O-H bond, which is due to the formation of Mo-O-H bonds and the inserted H_2O molecules.[38] The inserted protons likely bind terminal O of Mo-O bonds, elongating the terminal Mo-O bonds, where the structure contracts along the ***a*** axis, shortening the interlayer distance of (100) planes.[39,41] This contraction decreases the corner-sharing Mo-O bond distance, which results in a broad merged peak at around 1.47 Å with that of the terminal Mo-O bond length. The new peak at 2.2 Å belongs to the edge-sharing Mo-O bonds, which emerges due to elongation, where the results are in accord with XRD results, where the (020) planes expand their interlayer distance.

The peak separation for Mo-Mo distance is associated with inverse alternation of the corner and edge-sharing Mo-O bond, which also caused the opposite d-spacing evolution of (200) and (020) planes. After deprotonation, due to the elimination of the hydrogen bond, the corner-sharing Mo-O is elongated and the edge-sharing Mo-O bond is shortened, where these two peaks merge into a single peak, while the low oxidation state of Mo induces the remained right shift Mo-Mo peak. Combining with XRD results, the proton migrates via terminal oxygen instead of the Grotthuss mechanism through lattice water.

3. Conclusion

In summary, we have invented a new APB with concentrated H_3PO_4 as the electrolyte. The 9.5 m H_3PO_4 facilitates stable cycling and high rate capability of the MoO_3 electrode. The fast proton-diffusion kinetics through the electrode/electrolyte interface facilitates the fast rate capability, albeit of the diffusion-controlled migration of protons via terminal oxygens in MoO_3 anode. Integrating the H_3PO_4 electrolyte, the Grotthuss proton-conducting cathode of H-TBA, and the MoO_3 anode, the APB full cells display an outstanding low-temperature performance under -78 ^oC and even delivers power at -88 ^oC below the freezing point of 9.5 m H_3PO_4. It is interesting that APB is uniquely suitable at the low temperature of -78 ^oC because there are no problems with hydrogen evolution and self-discharge, and the cycling of APB does not fade even in the pouch cells. Importantly, the manufacturing of such APBs will be very competitive in cost and energy consumption as all cell components come from abundant sources. Such low-T APBs offer a safe and reliable option for aerospace and high-atmosphere missions, and this study blazes a trail for low-T aqueous batteries.

4. Experimental Section

Materials preparation: MoO_3 is prepared by a modified hydrothermal reaction.[42] Briefly, 1.0 g of $(NH_4)_6Mo_7O_{24}\cdot 4H_2O$ was dissolved in 25 mL de-ionized (DI) water before adding 10 mL HNO_3 (3 M) to adjust the pH to ca. 5. After stirring for 20 minutes, the transparent solution was transferred to a 40 mL autoclave, which was heated at 180 ^oC for 12 hrs. The obtained white powder was rinsed by DI water and centrifuged for multiple times before drying at 60 ^oC overnight. The chemically pre-protonated Turnbull's blue analogue (H-TBA) was synthesized by chemical reduction of $Cu_{II}[Fe_{III}(CN)_6]_{2/3}\cdot 4H_2O$.[43] For the preparation of $Cu_{II}[Fe_{III}(CN)_6]_{2/3}\cdot 4H_2O$, typically,

40 mL $CuSO_4$ solution (0.2 M) was added dropwise into 40 mL $K_3Fe(CN)_6$ solution (0.1 M) under stirring. After 6 hrs of reaction, the olive-green precipitate was washed by centrifuging for multiple times, which was then dried in an oven at 60 °C overnight. For the chemical reduction, the as-prepared powder was dispersed in 20 mL DI water (1g powder per100 mL) and sonicated for 10 minutes. Under N_2 protection, 10 mL hydrazine (0.05 M) solution was added dropwise to the above powder suspension under stirring. After reaction for 2 hrs, the crimson powder is washed by centrifuging for multiple times and dried in a vacuum oven overnight (40 ^oC).

Preparation of electrodes: The working electrodes for Swagelok® T-cells were composed of active material, super-P carbon (C65), and polyvinylidene fluoride (PVdF) binder (mass ratio: 7:2:1), which were coated on carbon fiber paper current collectors. For half-cell measurements, the counter electrodes were free-standing films comprising 70 wt.% activated carbon, 20 wt.% super-P carbon (C65), and 10 wt.% polytetrafluoroethylene (PTFE) binder. For full-cell measurements, the active mass loading for the MoO_3 anode is around 1.5 mg/cm^2, while it is ca. 2.3 mg/cm^2 for the H-TBA cathode. The free-standing MoO_3 electrode for *ex situ* characterization was prepared by mixing 70 wt.% of MoO_3, 20 wt.% of super-P carbon (C65), and 10 wt.% polytetrafluoroethylene (PTFE) binder. For pouch cells, the active material, super-P carbon (C65), and polyvinylidene fluoride (PVdF) binder (mass ratio: 7:2:1) were coated on titanium foil as the current collector with active mass loading around 4 mg/cm^2 for the MoO_3 anode and 6 mg/cm^2 for the H-TBA cathode.

Materials characterization: Ex situ synchrotron X-ray diffraction (XRD) patterns of MoO_3 were collected on the 11-ID-C beamline of the Advanced Photon Source (APS), Argonne National Laboratory, where the wavelength was 0.1173 Å. The Mo K-edge X-ray absorption spectroscopy (XAS) measurement was performed on the APS' bending-magnet beamline 9-BM-B with an

electron energy of 7 GeV and an average current of 100 mA. X-ray absorption near-edge structure (XANES) data reduction and analysis were processed by Athena software. The microstructure and morphology of MoO_3 nanoparticles were measured using FEI NOVA 230 field-emission scanning electron microscopy (FESEM) and FEI Titan 80-300 high-resolution transmission electron microscopy (HRTEM). The oxidation states of materials and electrodes were probed by X-ray photoelectron spectroscopy (XPS) *via* a Physical Electrons Quantera Scanning ESCA Microprobe with a focused monochromatic Al Kα X-ray (1486.6 eV) source for excitation. The Brunauer-Emmett-Teller (BET) method was measured to calculate the specific surface area using the adsorption branch. Thermogravimetric analyses (TGA) were performed on SDTQ600 Thermalanalyzer at a heating rate of 10 ^{o}C/min in Air.

Electrochemical measurements: The half-cell electrochemical properties were measured using Swagelok® three-electrodes T-cells (1/2-inch diameter) with the Ag/AgCl (3 M KCl) reference electrode (E = 0.210 vs standard hydrogen electrode, SHE) and glassy carbon rods to support current collectors. The electrolytes were H_3PO_4 acids of different concentrations, purged by N_2. Polyethylene sulfonate filter papers served as the separators. The galvanostatic charge/discharge (GCD) tests were measured on a Maccor system at room temperature. The cyclic voltammetry (CV) and Electrochemical Impedance Spectroscopy (EIS) were performed on a VMP-3 multi-channel workstation. For low-T measurements, the multi-temperature performance was measured in Thermotron 2800 oven for 25 ^{o}C and -40 ^{o}C. For tests at -78 ^{o}C, -84 ^{o}C and -88 ^{o}C the cells were submerged in the solid/liquid mixtures of CO_2(s)/isopropyl alcohol(l), ethyl acetate(s)/ethyl acetate(l) and isopropyl alcohol(s)/isopropyl alcohol(l), respectively, where these mixtures were contained in cryogenic storage dewars.

For **pouch cell construction**, the active materials were coated on rectangular Ti foils (2.0 cm × 1.5 cm). The pouch cells were assembled and sealed by an MSK-11A-S vacuum sealer, where these pouch cells were tested under constraining (Supplemental Information Digital image 1).

Symmetrical electrochemical impedance spectroscopy (EIS): Symmetrical EIS was conducted in a self-designed device as illustrated in Supplemental Information Schematic 1. Typically, two cells were assembled on both sides of the device with a waterproof barrier separating them, where one cell comprises MoO_3, activated carbon, and Ag/AgCl (3 M KCl) as working, counter and the reference electrode, respectively. The two cells were pre-cycled simultaneously but separately for three cycles. After pre-activation for three cycles, the MoO_3 electrodes in both cells were titrated to the same SOC, *i.e.*, half-protonated, before removing the barrier between the two cells to form a new electrochemical symmetrical cell with two MoO_3 electrodes for the EIS measurements. The EIS was conducted at room temperature in a frequency range from 50 mHz to 200 kHz. We analyzed the impedance data to evaluate the equivalent circuit parameters (modified Randles-type equivalent circuit) by using a parameter-fitting program (ZView® For Windows).

Electrochemical quartz crystal microbalance (EQCM): EQCM was carried out on a QCM200 quartz crystal microbalance.[44,45] Typically, 7 mg of MoO_3, 2 mg of super P carbon, and 3 mg of PVdF are mixed in 0.5 mL NMP. After sonicating for 1 hr, the slurry was sputtered on a 1-inch quartz crystal disk (O100RX3, p/n 6-615 Ti/Au, 5MHZ). *In situ* EQCM was measured simultaneously with CV measurements. The frequency change of the quartz resonator (Δf) was converted into a mass change (Δm) of the electrode coated on the quartz crystal by the Sauerbrey's equation:

$$\Delta m = \frac{\sqrt{\rho_q \mu_q}}{2 f_0} * \Delta f = -C_f * \Delta f \quad (1)$$

where ρ_q is the density of quartz (2.648 g/cm^3), μ_q is the shear modulus of quartz (2.947 × 1011 g/cm s^2), f_0 is the fundamental resonance frequency of the quartz, C_f is the sensitivity factor, and Δm and Δf are the mass change and frequency change, respectively. C_f is obtained by calculating the relation based on the frequency and mass change (measured by balance) between clean quartz and the coated electrodes. The value of the calibration constant used in this work is 16 ng/Hz, and the molar weight of charge carrier (M_w) was calculated by the equation below:

$$M_w = \frac{\Delta m\, n\, F}{\Delta Q} = \frac{C_f\,(-\Delta f)\, nF}{\Delta Q} \tag{2}$$

where F is Faraday constant (96485.33 C/mol) while n is the valence number of the ion. ΔQ is the Coulombs of charge pass through during the CV process.

Galvanostatic Intermittent Titration Technique (GITT): We performed a galvanostatic intermittent titration technique (GITT) measurements to monitor the kinetic change during the H^+ intercalation. We collected the GITT data at the first discharge and discharge after 10 cycles conditioning, with a current pulse at 100 mA/g for 5 min and a rest interval of 3 hrs. According to the equation (4), the diffusion coefficient in MoO_3 electrodes response to voltage can be determined:

$$\widetilde{D} = \frac{4}{\pi}\left(\frac{m_B V_M}{M_B S}\right)^2 \left(\frac{\Delta E_S}{\tau\left(dE_\tau/d\sqrt{\tau}\right)}\right)^2 \left(\tau \ll \frac{L^2}{D}\right) \tag{3}$$

V_M and M_B represent the molar volume and the molecular weight of the materials, respectively, while m_B and S are the mass and active surface area of the electrode, respectively. L is the average thickness of the electrode. If the cell voltage shows a linear relationship with $\tau^{1/2}$, the equation can be simplified as below:

$$\widetilde{D} = \frac{4}{\pi\tau}\left(\frac{m_B V_M}{M_B S}\right)^2 \left(\frac{\Delta E_S}{\Delta E_\tau}\right)^2 \tag{4}$$

where ΔE_τ is the total change of the cell voltage during the current pulse for the time τ and ΔE_s represents the change of the steady state voltage of the cell for the step at plateau potential.

Different scan-rate cyclic voltammetry (DSCV) with b value calculated: DSCV is conducted to understand the proton-storage kinetics, which can be characterized by analyzing the redox peak currents at various scan rates according to the equation: $i=av^b$.[46-48] Current *i* obeys a power-law relationship with the scan rate *v*, and ***a*** is an adjustment coefficient. The ***b***-value is determined from the slope of log(*i*) as a function of log(*v*). A ***b***-value of 0.5 represents the diffusion-controlled kinetics in a semi-infinite medium (Equation 5), whereas ***b***=1.0 indicates the redox behavior being non-diffusion controlled or capacitive (Equation 6).

$$i = nFAC^* D^{1/2} v^{1/2} \left(\frac{\alpha n_a F}{RT}\right)^{1/2} \pi^{1/2} \chi^{(bt)} \quad (5)$$

In Equation 5, C* represents the surface concentration of the electrode material, while R and D are the transfer and chemical diffusion coefficient. F, A, R, T, and n are the Faraday constant, surface area, molar gas constant, temperature, and the number of electrons involved, respectively. $\chi^{(bt)}$ denotes the normalized current for a totally irreversible system, as indicated by the cyclic voltammetric response.

$$|i_c| = AC_d v \quad (6)$$

In equation 6, i_c and C_d respond to current and capacitance, respectively

Supporting Information
Supporting Information is available from the Wiley Online Library or from the author.

Acknowledgments
X. Ji acknowledges the financial support from AID grant of Oregon State University. Work at Argonne National Laboratory was supported by the U. S. Department of Energy (DOE), Office of Energy Efficiency and Renewable Energy, Vehicle Technologies Office. Argonne National

Laboratory is operated for DOE Office of Science by UChicago Argonne, LLC, under contract number DE-AC02-06CH11357. This research used resources of the APS (9-BM and 11-ID-D), a US DOE Office of Science User Facility operated for the DOE Office of Science by Argonne National Laboratory under contract DE-AC02-06CH11357. M.A.S. acknowledges the financial support from US National Science Foundation (Award Number DMR 1508527). This work made use of instruments in the Electron Microscopy Service (OSU).

Received: ((will be filled in by the editorial staff))
Revised: ((will be filled in by the editorial staff))
Published online: ((will be filled in by the editorial staff))

References

[1] K. Xu, *Chem. Rev*. **2004**, *104*, 4303-4418.

[2] M. Armand, J. M. Tarascon, *Nature* **2008**, *451*, 652-657.

[3] C. Y. Wang, G. Zhang, S. Ge, T. Xu, Y. Ji, X. G. Yang, Y. Leng, *Nature* **2016**, *529*, 515-518.

[4] Q. Nian, J. Wang, S. Liu, T. Sun, S. Zheng, Y. Zhang, Z. Tao, J. Chen, *Angew. Chem. Int. Ed.* **2019**, *131*, 17150-17155.

[5] J. Holoubek, Y. Yin, M. Li, M. Yu, Y. S. Meng, P. Liu, Z. Chen, *Angew. Chem. Int. Ed.* **2019**, *58*, 18892-18897.

[6] C. S. Rustomji, Y. Yang, T. K. Kim, J. Mac, Y. J. Kim, E. Caldwell, H. Chun, Y. S. Meng, *Science* **2017**, *356*, eaal4263.

[7] Y. Yang, D. M. Davies, Y. Yin, O. Borodin, J. Z. Lee, C. Fang, M. Olguin, Y. Zhang, E. S. Sablina, X. Wang, C.S. Rustomji, Y. S. Meng, *Joule* **2019**, *3*, 1986-2000.

[8] X. Fan, X. Ji, L. Chen, J. Chen, T. Deng, F. Han, J. Yue, N. Piao, R. Wang, X. Zhou, X. Xiao, L. Chen, C. Wang, *Nat. Energy* **2019**, *4*, 882-890.

[9] X. Dong, Z. Guo, Z. Guo, Y. Wang, Y. Xia, *Joule* **2018**, *2*, 902-913.

[10] Y. Liang, Y. Jing, S. Gheytani, K. Y. Lee, P. Liu, A. Facchetti, Y. Yao, *Nat. Mater.* **2017**, *16*, 841-848.

[11] R. Emanuelsson, M. Sterby, M. Strømme, M. Sjödin, *J. Am. Chem. Soc.* **2017**, *139*, 4828-4834.

[12] X. Wang, Y. Xie, K. Tang, C. Wang, C. Yan, *Angew. Chem. Int. Ed.* **2018**, *57*, 11569-11573.

[13] X. Wu, J. J. Hong, W. Shin, L. Ma, T. Liu, X. Bi, Y. Yuan, Y. Qi, T. W. Surta, W. Huang, J. Neuefeind, T. Wu, P. A. Greaney, J. Lu, X. Ji, *Nat. Energy* **2019**, *4*, 123-130.

[14] L. Yan, J. Huang, Z. Guo, X. Dong, Z. Wang, Y. Wang, *ACS Energy Lett.* **2020**, *5*, 685−691.

[15] X. Wu, S. Qiu, Y. Xu, L. Ma, X. Bi, Y. Yuan, T. Wu, R. Shahbazian-Yassar, J. Lu, X. Ji, *ACS Appl. Mater. Interfaces* **2020**.

[16] Z. Guo, T. Wang, H. Wei, Y. Long, C. Yang, D. Wang, J. Lang, K. Huang, N. Hussain, C. Song, B. Guan, B. Ge, Q. Zhang, H. Wu, *Angew. Chem. Int. Ed.* **2019**, *131*, 12699-12703.

[17] D. Yu, K. Goh, H. Wang, L. Wei, W. Jiang, Q. Zhang, L. Dai, Y. Chen, *Nat. Nanotechnol.* **2014**, *9*, 555-562.

[18] K. R. Bullock, D. H. McClelland, *J. Electrochem. Soc.* **1977**, *124*, 1478-1482.

[19] H. R. Corti, F. J. Nores-Pondal, C. A. Angell, *Phys. Chem. Chem. Phys.* **2011**, *13*, 19741-19748.

[20] H. Kim, J. Hong, K. Y. Park, H. Kim, S. W. Kim, K. Kang, *Chem. Rev.* **2014**, *114*, 11788-11827.

[21] L. Suo, O. Borodin, T. Gao, M. Olguin, J. Ho, X. Fan, C. Luo, C. Wang, K. Xu, *Science* **2015**, *350*, 938-943.

[22] C. Yang, J. Chen, X. Ji, T. P. Pollard, X. Lü, C. J. Sun, S. Hou, Q. Liu, C. Liu, T. Qing, Y. Wang, O. Borodin, Y. Ren, K. Xu, C. Wang, *Nature* **2019**, *569*, 245-250.

[23] R. Schöllhorn, R. Kuhlmann, J. Besenhard, *Mater. Res. Bull.* **1976**, *11*, 83-90.

[24] N. Sotani, K. Eda, M. Sadamatu, S. Takagi, *Bull. Chem. Soc. Jpn.* **1989**, *62*, 903-907.

[25] J. Guo, P. Zavalij, M. S. Whittingham, *J. Solid State Chem.* **1995**, *117*, 323-332.

[26] D. Marx, M. E. Tuckerman, J. Hutter, M. Parrinello, *Nature* **1999**, *397*, 601-604.

[27] C. Chen, J. Liu, K. Amine, *J. Power Sources* **2001**, *96*, 321-328.

[28] R. Petibon, C. P. Aiken, N. N. Sinha, J. C. Burns, H. Ye, C. M. VanElzen, G. Jain, S. Trussler, J. R. Dahn, *J. Electrochem. Soc.* **2001**, *160*, A117-A124.

[29] A. Ramanujapuram, G. Yushin, *Adv. Energy Mater.* **2018**, *8*, 1802624.

[30] C. Yan, H. Li, X. Chen, X. Zhang, X. Cheng, R. Xu, J. Huang, Q. Zhang, *J. Am. Chem. Soc.* **2019**, *141*, 9422-9429.

[31] B. Kang, G. Ceder, *Nature* **2009**, *458*, 190-193.

[32] K. Xu, *Chem. Rev.* **2014**, *114*, 11503-11618.

[33] X. Han, Y. Gong, K. Fu, X. He, G. T. Hitz, J. Dai, A. Pearse, B. Liu, H. Wang, G. Rubloff, Y. Mo, V. Thangadurai, E. D. Wachsman, L. Hu, *Nat. Mater.* **2017**, *16*, 572-580.

[34] F. Wang, O. Borodin, M. Ding, M. Gobet, J. Vatamanu, X. Fan, T. Gao, N. Eidson, Y. Liang, W. Sun, S. Greenbaum, K. Xu, C. Wang, *Joule* **2018**, *2*, 927-937.

[35] F. Mo, Z. Chen, G. Liang, D. Wang, Y. Zhao, H. Li, B. Dong, C. Zhi, *Adv. Energy Mater.*, 2020, 2000035.

[36] L. Vilčiauskas, M. E. Tuckerman, G. Bester, S. J. Paddison, K. D. Kreuer, *Nat. Chem.* **2012**, *4*, 461-466.

[37] H. Jiang, J. J. Hong, X. Wu, T. W. Surta, Y. Qi, S. Dong, Z. Li, D. P. Leonard, J. Holoubek, J. C. Wong, J. J. Razink, X. Zhang, X. Ji, *J. Am. Chem. Soc.* **2018**, 140, 11556-11559.

[38] A. Michailovski, J. Grunwaldt, A. Baiker, R. Kiebach, W. Bensch, G. R. Patzke, *Angew. Chem. Int. Ed.* **2005**, *44*, 5643-5647.

[39] Y. Zhou, J. Ma, E. Hu, X. Yu, L. Gu, K. Nam, *Nat. Commun.* **2014**, *5*, 5381.

[40] T. Martin, Z. Derewenda, *Nat. Struct. Mol. Biol.* **1990**, *6*, 403.

[41] T. Ressler, R. E.Jentoft, J. Wienold, M. M. Günter, O. Timpe, *J. Phys. Chem. B* **2000**, *104*, 6360-6370.

[42] X. W. Lou, H. C. Zeng, *J. Am. Chem. Soc.* **2003**, *125*, 2697-2704.

[43] W. Hou, E. Wang, *Anal. Chim. Acta* **1992**, *257*, 275-280.

[44] D. A. Buttry, M. D. Ward, *Chem. Rev.* **1992**, *92*, 1355-1379.

[45] J. M. Griffin, A. C. Forse, W. Y. Tsai, P. L. Taberna, P. Simon, C. P. Grey, *Nat. Mater.* **2015**, *14*, 812.

[46] H. Lindström, S. Södergren, A. Solbrand, H. Rensmo, J. Hjelm, A. Hagfeldt, S. E. Lindquist, *J. Phys. Chem. B* **1997**, *101*, 7717-7722.

[47] J. Wang, J. Polleux, J. Lim, B. Dunn, *J. Phys. Chem. C* **2007**, *111*, 14925-14931.

[48] V. Augustyn, J. Come, M. A. Lowe, J. W. Kim, P. Taberna, S. H. Tolbert, H. D. Abruña, P. Simon, B. Dunn, *Nature Mater.* **2013**, *12*, 518-522.

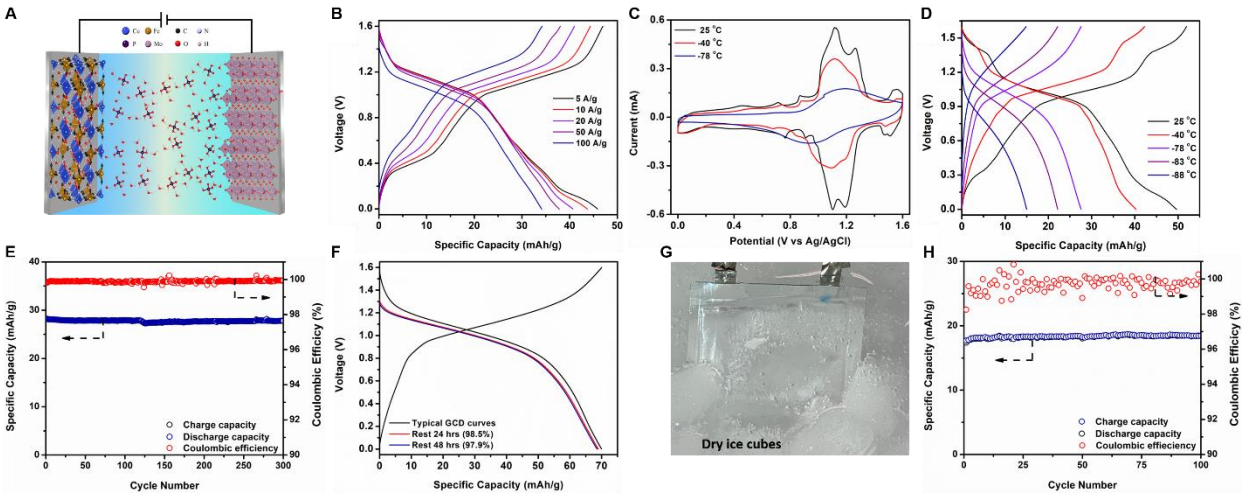

Figure 1. Electrochemical performance of APB under different temperatures. (A) Schematic of the APB device. **(B)** Rate performance of the APB from 5 to 100 A/g at 25 ºC. **(C)** CV curves of APBs at different temperatures at the scan rate of 1 mV/s**. (D)** Typical GCD potential profiles of APB at different temperatures at the current rate of 25 mA/g. **(E)** Cycling performance of APB at a current rate of 25 mA/g at -78 ºC over 300 cycles. **(F)** Self-discharge performance of APB at -78 ºC, with the discharge curves taken after resting at the open-circuit voltage for 24 hrs (red) and 48 hrs (blue). **(G)** Digital image of an APB operating under -78 ºC, where this temperature is obtained by the solid/liquid mixture of dry ice cubes in isopropyl alcohol. **(H)** Cycling performance of an APB pouch cell at a current rate of 20 mA/g at -78 ºC.

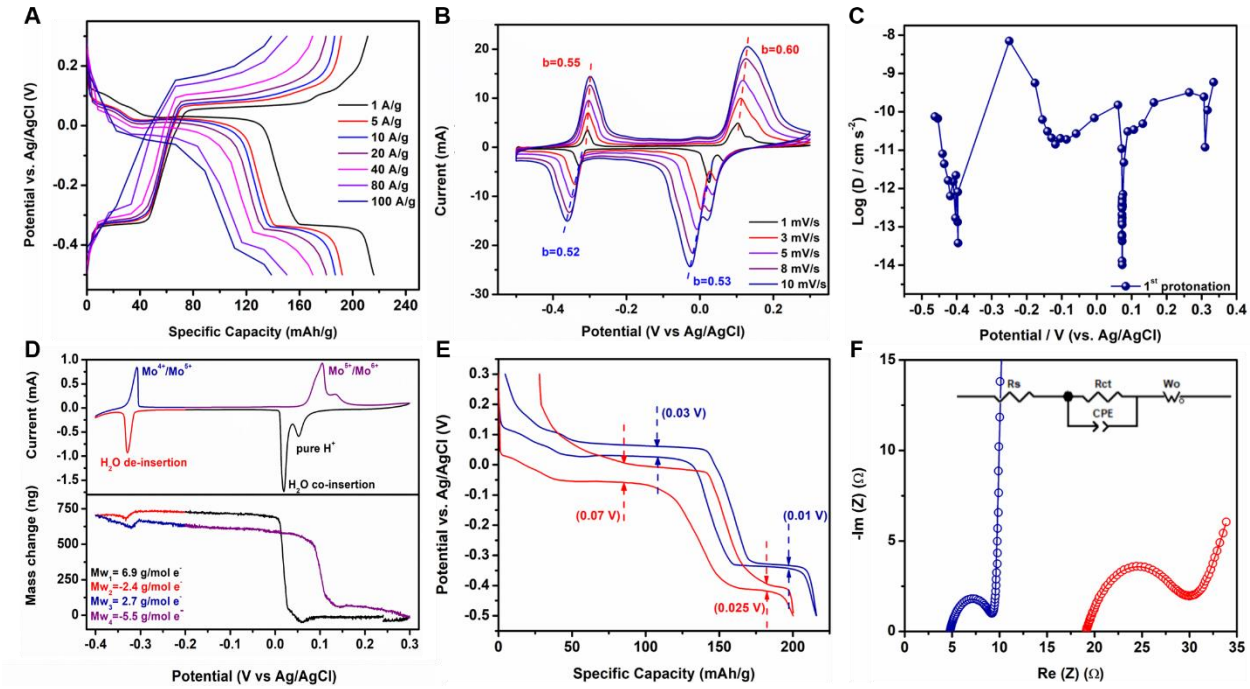

Fig. 2 Kinetic study of the MoO_3 anode in 9.5 m H_3PO_4 electrolyte. (A) Rate performance from 1 to 100 A/g. **(B)** CV curves at scan rates from 1 to 10 mV/s, where *b*-values are calculated. **(C)** The GITT profile from the 1st protonation. **(D)** A typical CV curve at 3 mV/s (top) and its corresponding EQCM profile (bottom). **(E)** Hysteresis voltage comparison of 9.5 m H_3PO_4 (royal) and 1 M H_3PO_4 electrolyte (red) in GCD potential profiles. **(F)** Typical Nyquist plots in 9.5 m H_3PO_4 (royal) and 1 M H_3PO_4 electrolyte (red). Inset: the equivalent circuit for fitting.

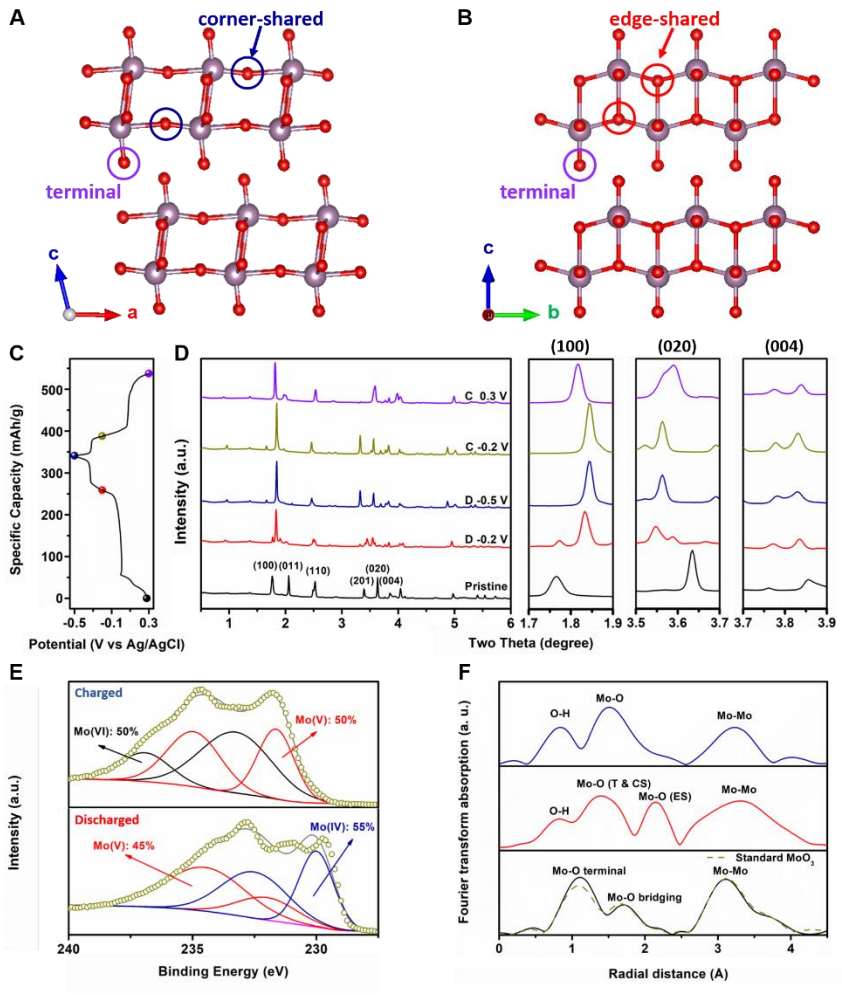

Figure 3. Characterization of the proton-storage mechanism in the MoO_3 electrode in 9.5 m H_3PO_4 electrolyte. Schematic of the MoO_3 crystal structure along **(A)** ***b*** axis and **(B)** ***a*** axis. **(C)** The GCD potential profiles of the first cycle. **(D)** The *ex situ* synchrotron XRD patterns of the MoO_3 electrode at different SOC in the first cycle corresponding to points marked in **c**. Left: full pattern. Right: magnified pattern for (100), (020), and (004) peaks. **(E)** *Ex situ* XPS Mo 2p spectra of the MoO_3 electrode at two SOC: discharged to -0.5 V (upper) and charged to 0.3 V (bottom).**(F)** *Ex situ* Fourier-transform Mo-K edge EXAFS spectra of standard MoO_3 powder (dark yellow), pristine (black), fully charged (red), and fully discharged (royal) samples, where T, ES, and CS in the figure are short for the terminal, edge-sharing, and corner-sharing, respectively.

The table of contents shows that aqueous proton battery (APB) full cells demonstrate outstanding low-temperature performance via 62 w% (9.5 m) H_3PO_4 as the electrolyte that does not freeze until -85 ºC. At -78 ºC, the APB delivers negligible capacity fading over **300** cycles and high rate capability. The high-performing pouch cells reach an advanced technology readiness level, thereby being very promising for aerospace and high-atmosphere applications.

Keyword: *Battery, Low temperature, Proton, Phosphoric acid, Aqueous electrolyte*

*Heng Jiang, Woochul Shin, Lu Ma, Jessica J. Hong, Zhixuan Wei, Yusung Liu, Suoying Zhang, Xianyong Wu, Yunkai Xu, Qiubo Guo, Mas A. Subramanian, William F. Stickle, Tianpin Wu, Jun Lu *, Xiulei Ji**

A high-rate aqueous proton battery delivering power below -78 ºC via an unfrozen phosphoric acid

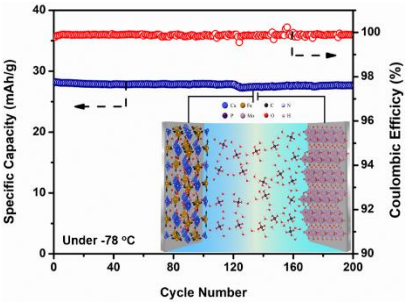

Supporting Information

A high-rate aqueous proton battery delivering power below -78 °C via an unfrozen phosphoric acid

*Heng Jiang, Woochul Shin, Lu Ma, Jessica J. Hong, Zhixuan Wei, Yusung Liu, Suoying Zhang, Xianyong Wu, Yunkai Xu, Qiubo Guo, Mas A. Subramanian, William F. Stickle, Tianpin Wu, Jun Lu *, Xiulei Ji**

H. Jiang, W. Shin, J. J. Hong, Dr. Z. Wei, Y. Liu, Dr. X Wu, Y. Xu, Q. Guo, Prof. M. A. Subramanian, and Prof. X. Ji

Department of Chemistry, Oregon State University, Corvallis, 97331-4003, United States

*Email: david.ji@oregonstate.edu

Dr. J. Lu

Chemical Sciences and Engineering Division and X-ray Science Division, Advanced Photon Sources, Argonne National Laboratory, Lemont, IL, 60439, United States

*Email: junlu@anl.gov

Dr. L. Ma, Dr. S. Zhang, Dr. T. Wu

X-ray Science Division, Advanced Photon Sources, Argonne National Laboratory, Lemont, Illinois, 60439, United States

Dr. W. Stickle

Hewlett-Packard Co. 1000 NE Circle Blvd., Corvallis, OR 97330, United States

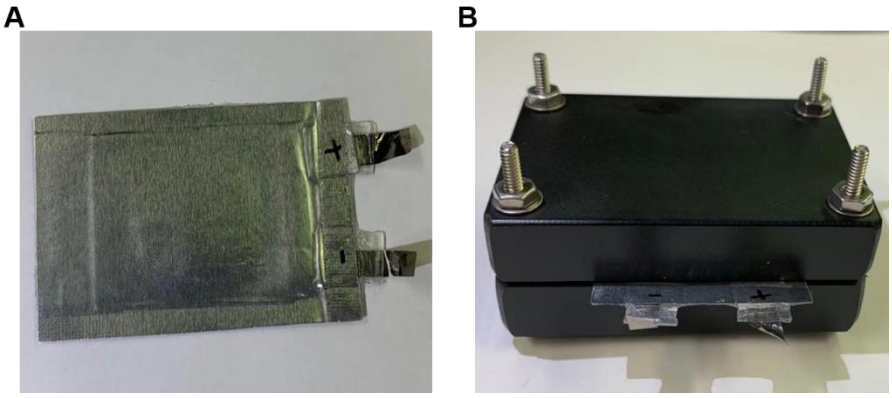

Digital image 1. (A) An as-assembled pouch cell and **(B)** A pouch cell under constraining.

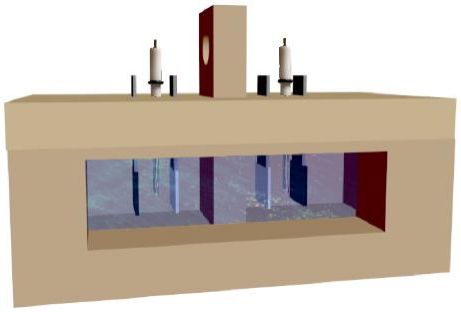

Schematic 1. Symmetric battery setting for the EIS measurements. In the left section, the electrodes of activated carbon, Ag/AgCl reference, and MoO_3 are placed from left to right; in the right section, this stacking sequence of the three electrodes are reversed.

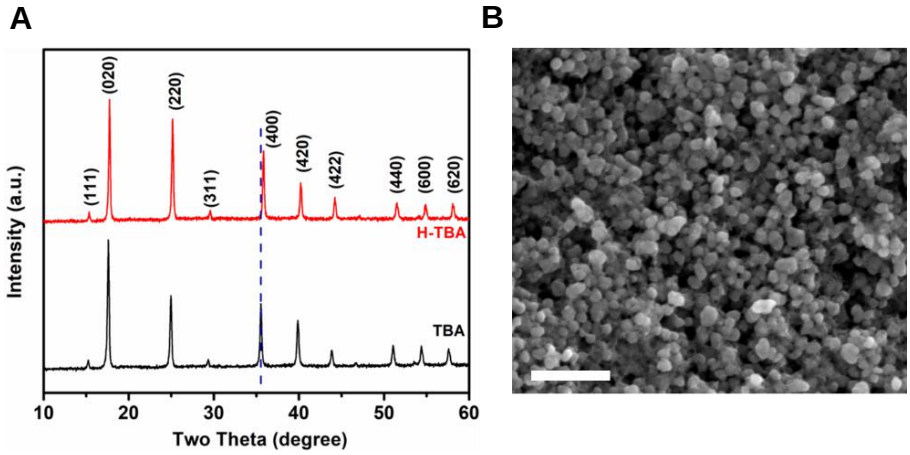

Figure S1. Physical characterization of chemically pre-protonated Turnbull's blue analogue—$H_xCu^{II}[Fe^{III}(CN)_6]_{2/3}\cdot 4H_2O$ (H-TBA). (A) An XRD pattern with peak identification. **(B)** An SEM image. Scale bar, 2 μm.

Supplementary Note: **Figure S1** demonstrates the physical characterizations of the as-prepared H-TBA. After the chemical reduction in hydrazine, the crystal structure of TBA is maintained with a slight right shift of (004) peak due to the reduction of $[Fe(CN)_6]^{3-}$ during proton insertion (**Figure S1A**).[1,2] The as-prepared H-TBA exhibits a uniform nano-cube structure with length around 250 nm (**Figure S1B**).

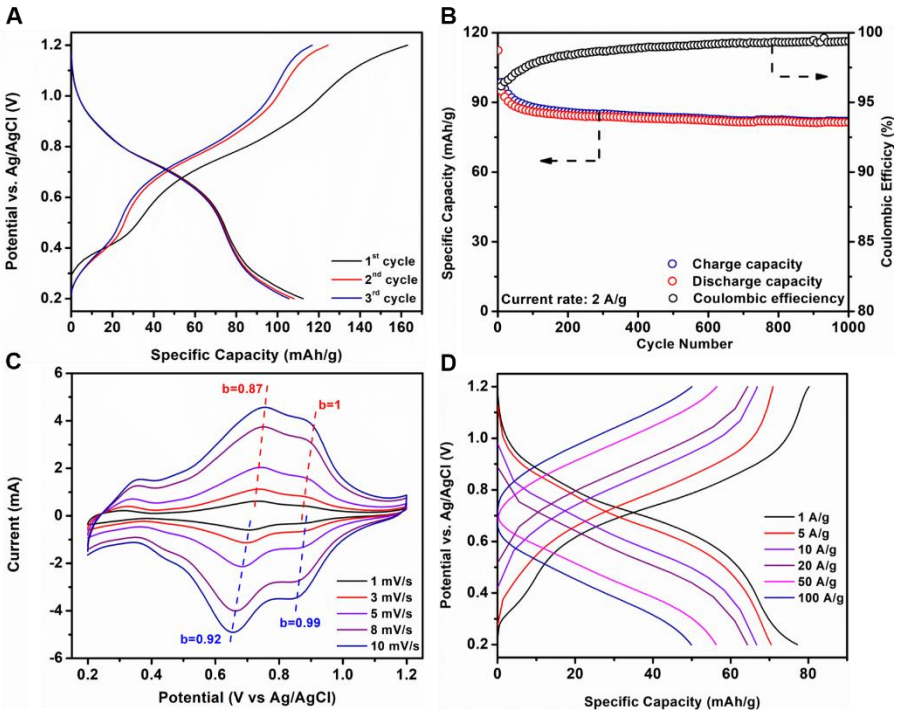

Figure S2. Electrochemical performance of chemically pre-protonated Turnbull's blue analogue—$H_xCu^{II}[Fe^{III}(CN)_6]_{2/3}\cdot 4H_2O$ (H-TBA): **(A)** Typical GCD potential profiles for the initial three cycles at a current rate of 2 A/g. **(B)** Cycling performance at 2 A/g for 1000 cycles. **(C)** CV curves obtained at different scan rates with b-values. Sweep rates are varied from 1 to 10 mV/s. **(D)** Rate performance from 1 A/g to 100 A/g.

Supplementary Note: **Figure S2** shows the electrochemical performance of the as-prepared H-TBA. Galvanostatic charge/discharge (GCD) potential profiles of the H-TBA electrode in 9.5 m H_3PO_4 electrolyte shows a first de-protonation capacity of 163 mAh/g at the current rate of 2 A/g, which corresponds to 1.5 protons per formula (**Figure S2A**). The following discharge capacity is 112 mA/g, and H-TBA exhibits a stable cycle life for 1000 cycles with 86% capacity retention (**Figure S2B**). The calculated ***b***-values of four primary peaks are nearly unity, indicating the non-diffusion-controlled proton (de)insertion during redox reactions of H-TBA (**Figure S2C**). The fast

kinetics of the proton diffusion endows the high rate performance, where high capacity utilization of 60% is still attainable at a current rate of 100 A/g (**Figure S2D**)

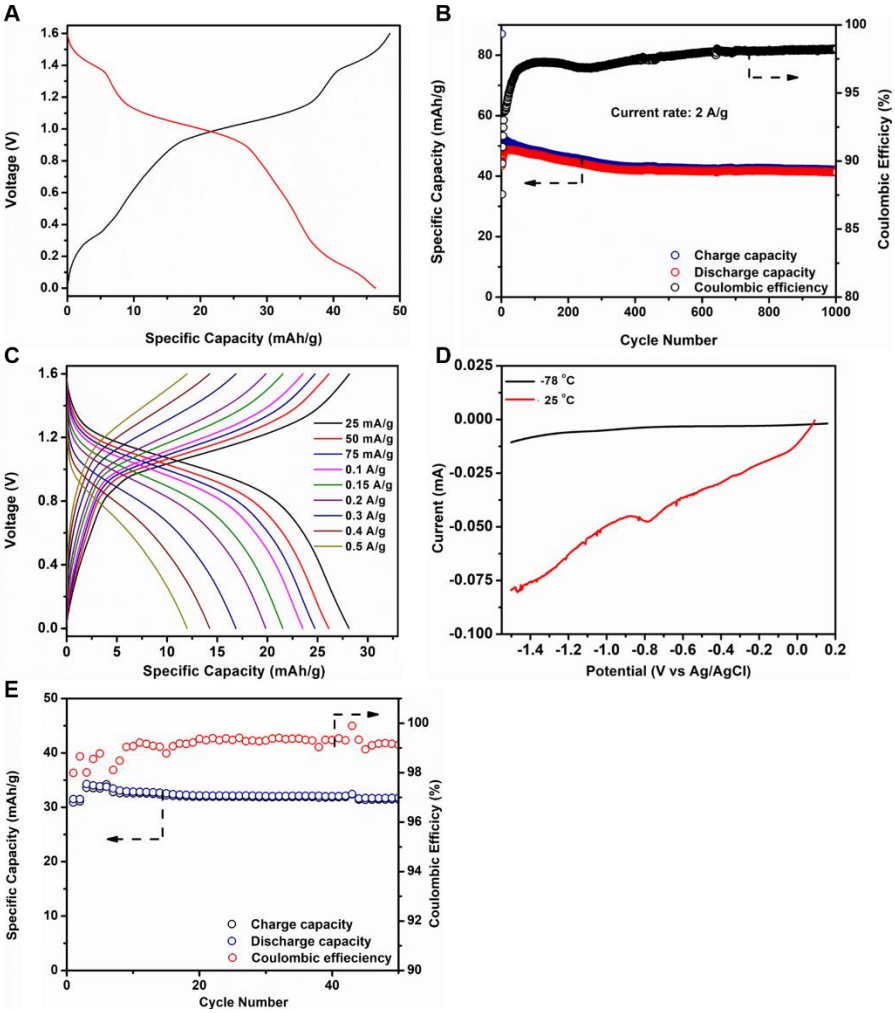

Figure S3. Electrochemical performance of APBs in the 9.5 m H_3PO_4 electrolytes under different temperatures. (A) Typical GCD potential profile of APBs full cell under the current rate of 2 A/g at 25 ºC. **(B)** Cycling performance of APBs under the current rate of 2 A/g for 1000 cycles at 25 ºC. **(C)** Rate performance of APBs in the 9.5 m H_3PO_4 electrolyte from 25 to 500 mA/g under -78 ºC. **(D)** Linear sweep voltammetry (LSV) of the 9.5 m H_3PO_4 electrolyte under different temperatures at the scan rate of 1 mV/s. **(E)** Cycling performance of APPCs under a current rate of 50 mA/g at -40 ºC for 50 cycles.

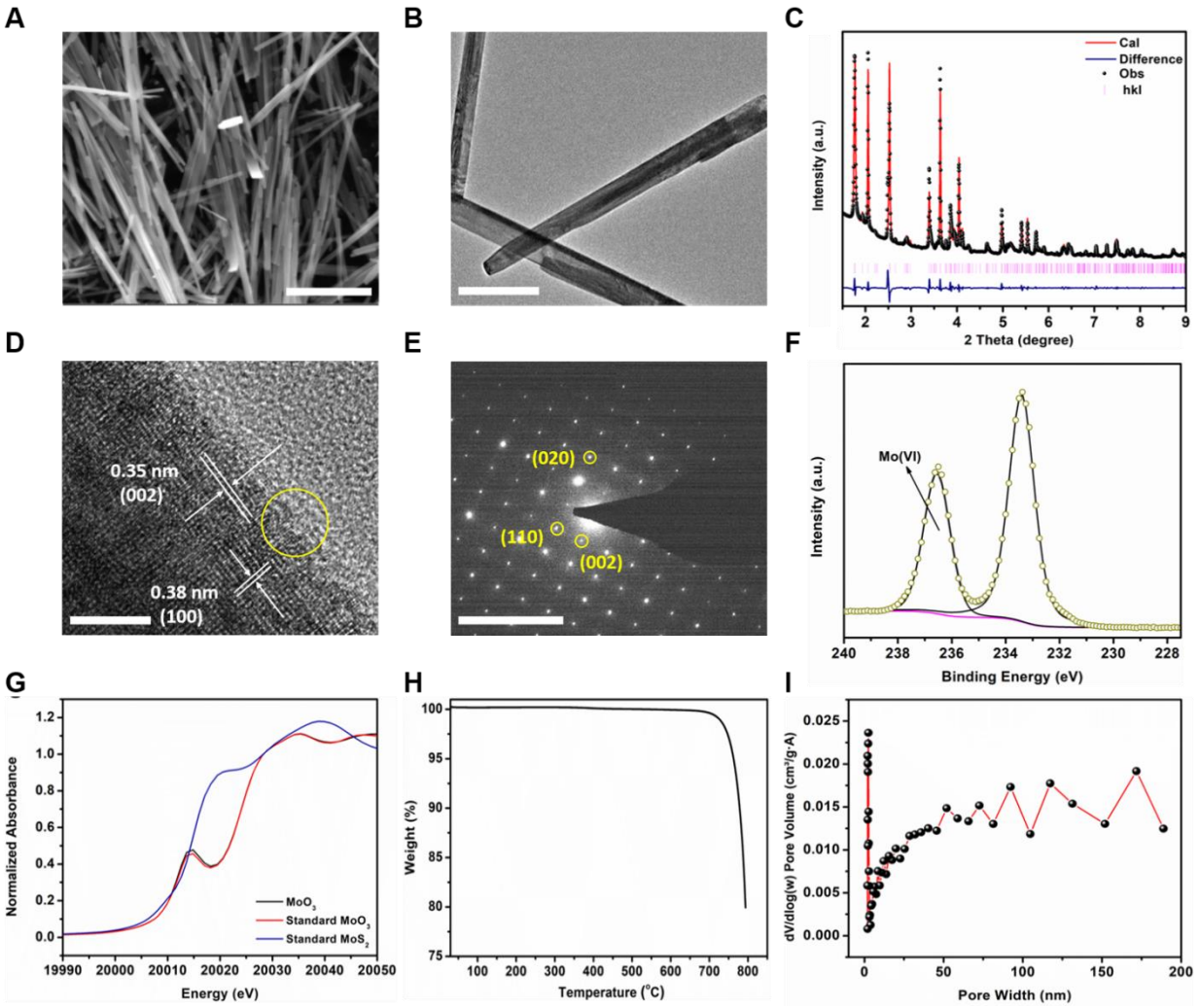

Figure S4. Physical characterizations of MoO_3 powder. **(A)** SEM image. Scale bar, 5 μm. **(B)** TEM image. Scale bar, 1 μm. **(C)** The synchrotron XRD patterns and Rietveld refinement of MoO_3 nanorods. **(D)** HRTEM image with lattice identified. Scale bar, 5 nm. **(E)** The SAED pattern of the selected area in **D**. Scale bar, 10 1/nm. **(F)** The XPS Mo 2p spectrum. **(G)** Normalized XANES spectrum. **(H)** TGA curve under Ar atmosphere; **(I)** Pore size distribution from BET measurement.

Supplementary Note: **Figure S4** displays the results of the physical characterization of the as-prepared MoO_3. MoO_3 comprises nanofibers, ~ 5 μm long and ~ 20 nm wide, as shown in images of scanning electron microscopy (SEM) and transmission electron microscopy (TEM) in **Figure**

S4A and **B**. The synchrotron X-ray diffraction (XRD) patterns exhibit a monoclinic crystal structure with Rietveld refined lattice parameters of a=3.96, b=3.70, c=7.19 (**Figure S4C**). A high-resolution TEM (HRTEM) image reveals the d-spacing of the lattice matching with (002) and (100) planes of MoO_3, which depicts the orientation of the nanofiber along the *b* axis (**Figure S4D**). The selected area electron diffraction (SAED) displays the lattice plane matching with the refinement data (**Figure S4E**). The XPS confirms the oxidation state of Mo (VI) with the $3d_{3/2}$ and $3d_{5/2}$ binding energies at 233.5 and 236.5 eV, respectively (**Figure S4F**), which is accord with result of Mo-K edge XANES spectrum (**Figure S4G**).[3-5] TGA exhibits the hydrophobic properties of MoO_3 and the mass loss at the high-temperature range due to the evaporation of metal oxide (**Figure S4H**). N_2 sorption studies reveal the Brunauer-Emmett-Teller (BET) surface area of ~8 m^2/g and a broad pore size distribution (**Figure S4I**).

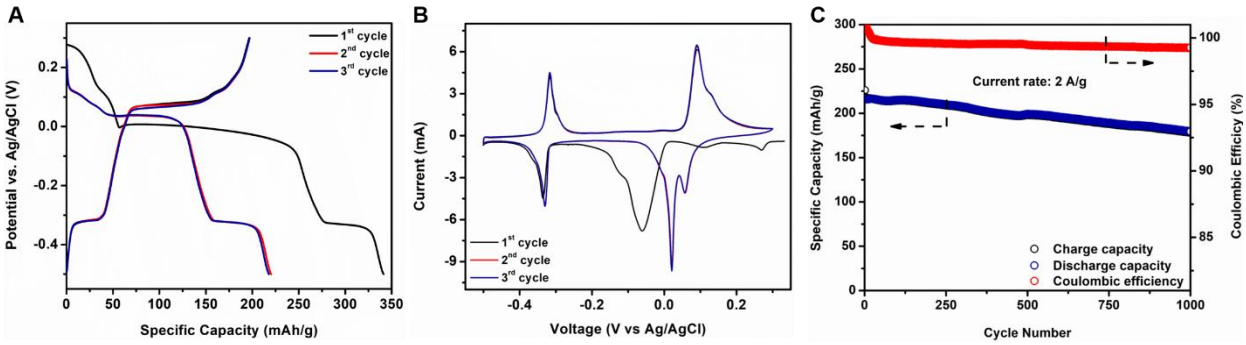

Figure S5. Electrochemical performance of the MoO_3 electrode in 9.5 m H_3PO_4 electrolyte. **(A)** The GCD potential profiles in the first three cycles. **(B)** The CV curves of the initial three cycles. **(C)** Cycling performance with Coulombic efficiency at the current rate of 2 A/g.

Supplementary Note: **Figure S5** exhibits the electrochemical performance of the MoO_3 electrode in the 9.5 m H_3PO_4 electrolyte. In Swagelok® cells with activated carbon and Ag/AgCl (3 M HCl) as the counter and the reference electrode, galvanostatic charge/discharge (GCD) cycling was carried out at a current rate of 1 A/g between -0.5 to 0.3 V vs. Ag/AgCl. The initial GCD potential profile reveals a discharge capacity of 341 mAh/g with Coulombic efficiency (CE) of 57%, where the profile exhibits two distinct plateaus at around 0 and -0.32 V corresponding to Mo^{6+}/Mo^{5+} and Mo^{5+}/Mo^{4+} redox reactions (**Figure S5A**). The following cycles show three reduction reactions at 0.035, 0, and -0.34 V with corresponding oxidation reactions at 0.1, 0.08, and -0.32 V, respectively, which conforms to cyclic voltammetry (CV) curves (**Figure S5B**). Due to the low water content, the 9.5 m H_3PO_4 electrolyte demonstrates a stable cycling performance with ~82% capacity maintained for 1000 cycles at the current rate of 2 A/g (**Figure S5C**).

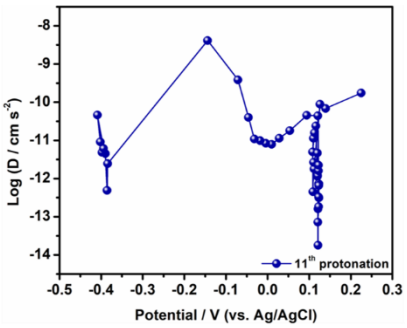

Figure S6. GITT profile of the MoO_3 anode in the 11th discharge.

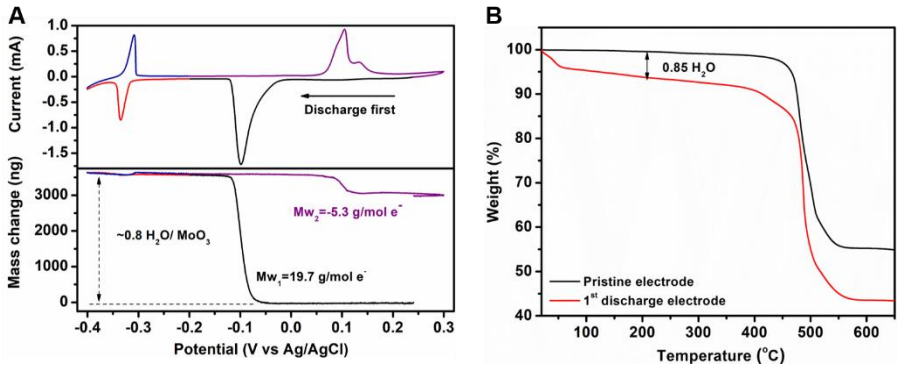

Figure S7. Water trapping in the structure of MoO_3. (A) The CV curve of the MoO_3 electrode in the first cycle at a scan rate of 3 mV/s (top) and its corresponding EQCM profiles (bottom). **(B)** The TGA of MoO_3 at different state of charge (SOC). Black: OCV, red: first discharge to -0.5 V.

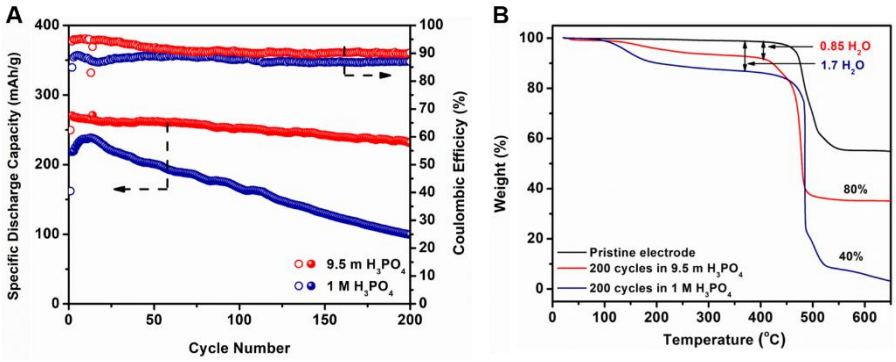

Figure S8. Comparison of cycling performance of the MoO_3 anode in different electrolytes. **(A)** Cycling performance at a low current rate of 0.2 A/g in 9.5 m H_3PO_4 and 1 M H_3PO_4. **(B)** Corresponding TGA of MoO_3 electrodes after 200 cycles in different electrolytes.

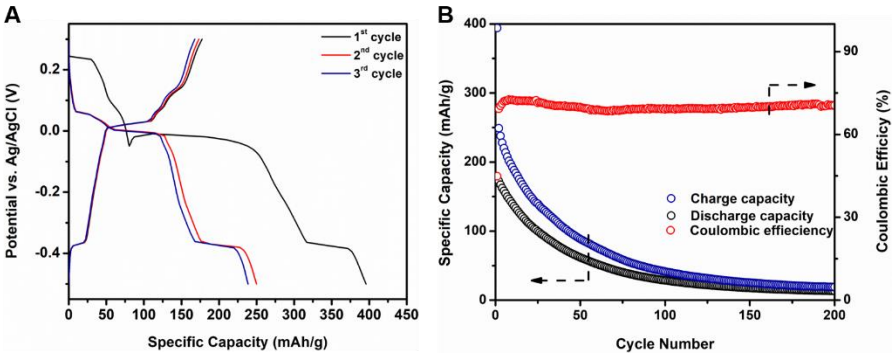

Figure S9. Electrochemical performance of the MoO_3 electrode in 1 M H_2SO_4. (A) GCD potential profiles in the first three cycles. **(B)** Cycling performance with Coulombic efficiency at the current rate of 200 mA/g for 25 cycles.

Extended Data Table 1. Recent progress on low-temperature batteries below -40 ºC.

Cathode	Anode	Electrolyte	Temp.	Capacity at the Lowest T vs. Room temperature capacity	Low-T full cell cycling/ retention	Low-T pouch cell performance
$Li_3V_2(PO_4)_3$	Mg	PhMgCl+$AlCl_3$+LiCl+THF	-40 ºC	47%	N/A	N/A [6]
S	Li	0.5 M $LiCF_3SO_3$+0.5 M $LiNO_3$ in DOL/DME	-40 ºC	41%	N/A	N/A [7]
$Li_3V_2(PO_4)_3$	Li_xC	1M $LiPF_6$ in EC/EMC/DMC	-40 ºC	67%	N/A	N/A [8]
$Na_3V_2(PO_4)_3$@C	AC	2 M $NaClO_4$ in DI with 0.3 mole fraction of DMSO	-50 ºC	61%	N/A	N/A [9]
Polyimide	PI	5 m LiTFSI/EA + DCM (1:4 V)	-70 ºC	69%	100 cycles/76% (-70 ºC)	N/A [10]
$LiCoO_2$	Li	2 M LiTFSI in DM:CO_2 (19:1)	-78 ºC	61%	N/A	N/A [11]
$LiCoO_2$	$LiTiO_2$	0.75 M LiTFSI in 1,3-dioxane	-80 ºC	65%	N/A	N/A [12]
LMO	LTPO	2 M LiTFSI in EA	-70 ºC	70%	N/A	N/A [13]
Graphite	Graphite	2 M LiTFSI in MP with 10% FEC	-60 ºC	85%	N/A	N/A [14]
$LiNi_{0.8}Co_{0.15}Al_{0.05}O_2$	Li	LiBETI-FEC/DEC or LiTFSI- FEC/FEMC into D2 or M3	-85 ºC	50%	450 cycles/88% (-20 ºC)	Yes but no cycling [15]
$Na_{0.7}[Mn_{0.6}Ni_{0.2}Mg_{0.2}]O_2$	$CoGa_2S_4$ @G	0.5 M $NaSO_3CF_3$ in 1,2-dimethoxyethane	-60 ºC	42%	1000 cycles/28% (-60 ºC)	N/A [16]
$LiNi_{0.8}Co0.15Al_{0.05}O_2$	graphite	1 M $LiPF_6$ in EC-PC-EMC mixture	-40 ºC	68%	100 cycles/95% (-40 ºC)	Yes/ 40 cycles [17]
PI5	PTPAn	1 M EMITFSI MA/AN (1/2, v/v)	-80 ºC	79%	N/A	N/A [18]
RGO	K	0.8 M KPF_6 in EC: PC (1:1)	-40 ºC	58%	N/A	N/A [19]
$LiNi_{0.5}Mn_{1.5}O_4$	MCMB	1 M $LiPF_6$ in MA/EC/DEC/EMC (3:1:1:1)	-60 ºC	40%	500 cycles/90% (-20 ºC)	N/A [20]
LTO	CNT	0.75 M LiTFSI in DIOX	-60 ºC	70%	N/A	N/A [21]
Graphite	Li	0.75 M LiTFSI in DIOX	-40 ºC	47%	N/A	N/A [22]
MnO_2	MoO_3	2 M H_2SO_4 plus 2 M $MnSO_4$ in solid state electrolyte (solid)	-70 ºC	81.5%	100 cycles	N/A [23]
MnO_2	PTO	2 M H_2SO_4 plus 2 M $MnSO_4$ in solid state electrolyte (solid)	-70 ºC	73%	100 cycles/99% (-70 ºC)	N/A [24]
NiFe-TBA	AC	1 M H_2SO_4 (solid)	-40 ºC	89%	N/A	N/A [25]
H-TBA	**MoO_3**	**9.5 m H_3PO_4**	**- 78 ºC**	**55%**	**200 cycles/98% (-78 ºC)**	**Yes/100 cycles (this work)**

Reference:

[1] X. Wu, J. J. Hong, W. Shin, L. Ma, T. Liu, X. Bi, Y. Yuan, Y. Qi, T. W. Surta, W. Huang, J. Neuefeind, T. Wu, P. A. Greaney, J. Lu, X. Ji, *Nat. Energy*, **2019**, *4*, 123-130.

[2] C. D. Wessells, R. A. Huggins, Y. Cui, *Nat. Commun.*, **2011**, *2*, 550.

[3] H. S. Kim, J. B. Cook, H. Lin, J. S. Ko, S. H. Tolbert, V. Ozolins, B. Dunn, *Nat. Mater.*, **2017**, *16*, 454-460.

[4] X. Wang, Y. Xie, K. Tang, C. Wang, C. Yan, *Angew. Chem. Int. Ed.* **2018**, *57*, 11569-11573.

[5] A. Michailovski, J. D. Grunwaldt, A. Baiker, R. Kiebach, W. Bensch, G. R. Patzke, *Angew. Chem. Int. Ed.*, **2005**, *44*, 5643-5647.

[6] M. Rashad, H. Zhang, X. Li, H. Zhang, *J. Mater. Chem. A*, **2019**, *7*, 9968-9976.

[7] D. R. Deng, F. Xue, C. D. Bai, J. Lei, R. Yuan, M. S. Zheng, Q. F. Dong, *ACS Nano*, **2018**, *12*, 11120-11129.

[8] Y. Liu, B. Yang, X. Dong, Y. Wang, Y. Xia, *Angew. Chem. Int. Ed.*, **2017**, *56*, 16606-16610.

[9] Q. Nian, J. Wang, S. Liu, T. Sun, S. Zheng, Y. Zhang, Z. Tao, J. Chen, *Angew. Chem. Int. Ed.*, **2019**, *131*, 17150-17155.

[10] X. Dong, Y. Lin, P. Li, Y. Ma, J. Huang, D. Bin, Y. Wang, Y. Qi, Y. Xia, *Angew. Chem. Int. Ed.*, **2019**, *131*, 5679-5683.

[11] C. S. Rustomji, Y. Yang, T. K. Kim, J. Mac, Y. J. Kim, E. Caldwell, H. Chung, Y. S. Meng, *Science*, **2017**, *356*, eaal4263.

[12] J. Xu, X. Wang, N. Yuan, J. Ding, S. Qin, J. M. Razal, X. Wang, S. Ge, Y. Gogotsi, *Energy Storage Mater.*, **2019**, *23*, 383-389.

[13] X. Dong, Z. Guo, Z. Guo, Y. Wang, Y. Xia, *Joule*, **2018**, *2*, 902-913.

[14] J. Holoubek, Y. Yin, M. Li, M. Yu, Y. S. Meng, P. Liu, Z. Chen, *Angew. Chem. Int. Ed.*, **2019**, *58*, 18892-18897.

[15] X. Fan, X. Ji, L. Chen, J. Chen, T. Deng, F. Han, J. Yue, N. Piao, R. Wang, X. Zhou, X. Xiao, L. Chen, C. Wang, *Nat. Energy*, **2019**, *4*, 882-890.

[16] F. Mo, Z. Lian, B. Fu, Y. Song, P. Wang, F. Fang, Y.-N. Zhou, S. Peng, D. Sun, *J. Mater. Chem. A*, **2019**, *7*, 9051-9058.

[17] Q. Li, D. Lu, J. Zheng, S. Jiao, L. Luo, C. M. Wang, K. Xu, J. G. Zhang, W. Xu, *ACS Appl. Mater. Interfaces*, **2017**, *9*, 42761-42768.

[18] J. Qin, Q. Lan, N. Liu, Y. Zhao, Z. Song, H. Zhan, *Energy Storage Mater.*, **2019**.

[19] Y. Wang, X. Gao, L. Li, M. Wang, J. Shui, M. Xu, *Nano Energy*, **2020**, *67*, 104248.

[20] G. Xu, S. Huang, Z. Cui, X. Du, X. Wang, D. Lu, X. Shangguan, J. Ma, P. Han, X. Zhou, *J. Power Sources*, **2019**, *416*, 29-36.

[21] B. Hu, X. Zhou, J. Xu, X. Wang, N. Yuan, S. Ge, J. Ding, *ChemElectroChem*, **2020**, *7*, 716-722.

[22] J. Xu, X. Wang, N. Yuan, B. Hu, J. Ding, S. Ge*, J. Power Sources*, **2019**, *430*, 74-79.

[23] L. Yan, J. Huang, Z. Guo, X. Dong, Z. Wang, Y. Wang, *ACS Energy Lett.*, **2020**, *5*, 685-691.

[24] Z. Guo, J. Huang, X. Dong, Y. Xia, L. Yan, Z. Wang, Y. Wang, *Nat. Commun.*, **2020**, *11*, 1-9.

[25] X. Wu, S. Qiu, Y. Xu, L. Ma, X. Bi, Y. Yuan, T. Wu, R. Shahbazian-Yassar, J. Lu, X. Ji, *ACS Appl. Mater. Interfaces*, **2020**.